Nano Energy 40 (2017) 73–81

Contents lists available at ScienceDirect

Nano Energy

journal homepage: www.elsevier.com/locate/nanoen

Full paper

Nanoribbons and nanoscrolls intertwined three-dimensional vanadium oxide hydrogels for high-rate lithium storage at high mass loading level

Yuhang Dai[a,1], Qidong Li[a,1], Shuangshuang Tan[a,1], Qiulong Wei[a,b,*], Yexin Pan[a], Xiaocong Tian[d], Kangning Zhao[a], Xu Xu[a], Qinyou An[a], Liqiang Mai[a,c,*], Qingjie Zhang[a]

[a] State Key Laboratory of Advanced Technology for Materials Synthesis and Processing, International School of Materials Science and Engineering, Wuhan University of Technology, Wuhan 430070, China
[b] Department of Materials Science and Engineering, University of California, Los Angeles, CA 90095, USA
[c] Department of Chemistry, University of California, Berkeley, CA 94720, USA
[d] Singapore Centre for 3D Printing, School of Mechanical and Aerospace Engineering, Nanyang Technological University, 639798 Singapore, Singapore

ARTICLE INFO

Keywords:
Vanadium oxide
Hydrogel
Lithium ion battery
Flexible film
Hybrid 3D structure

ABSTRACT

Ultrathin layered nanomaterials show promising advantages to promote the Li^+ diffusion kinetics, however, the self-aggregation/stacking of nanomaterials lead to large capacity loss and limited rate capability, which urgently needs to be addressed. Herein, we report a three-dimensional (3D) novel vanadium oxide ($H_2V_3O_8$) hydrogel nanostructure composed of intertwined ultrathin nanoribbons and self-coiled nanoscrolls, synthesized by a universal modified liquid exfoliation method. The hydrogels display largely enhanced rate capability and cycling stability, compared to those of the pure nanowires and nanoribbons. Based on the geometrical features of hydrogels, the intertwined hydrogels/carbon nanotubes (CNTs) flexible film is fabricated and delivers remarkable lithium storage performance: a high capacity of 310 mA h g^{-1} at 0.1 A g^{-1}, excellent rate capability (145 mA h g^{-1} at 12 A g^{-1}) and stable cycling performance. Moreover, at a high mass loading up to 13 mg cm^{-2}, the hydrogels/CNTs film delivers an area capacity ~ 2.7 mA h cm^{-2} (at 0.91 mA cm^{-2}), high rate capability (an area capacity of 1.16 mA h cm^{-2} at 18.2 mA cm^{-2}). The scalable hydrogels/CNTs films provide a promising route towards high performance flexible electrodes at high mass loading.

1. Introduction

Electrical energy storage (EES) is indispensable in our daily life which has been applied widely in portable electronics [1–4]. Li-ion batteries (LIBs) are one of the best candidates, but their performance is expected to be further improved [5–9]. Developing electrode materials with high capacity, fast charging and long lifespan is necessary [1,3,8]. Vanadium oxides are attractive electrode materials due to the high theoretical capacity (multi-electron reaction with a high capacity over 300 mA h g^{-1}) and abundant source [10–17]. However, the low electrical conductivity and sluggish reaction kinetics of vanadium oxides hinder their widespread applications. Among various types of layered vanadium oxides, $H_2V_3O_8$ is consisted of V_3O_8 layers (comprised of VO_6 octahedrons and VO_5 trigonal bipyramids) with large layer spacing, which act as the host for Li^+ ion intercalation [13,18–20]. Meanwhile, $H_2V_3O_8$ contains mixed valences of V^{5+} and V^{4+}, while hydrogen atoms are linked with VO_6 through hydrogen bonds to connect the V_3O_8 layers, which provides good electronic conductivity for high rate charge/discharge [20]. These properties endow the $H_2V_3O_8$ as a promising candidate for high-performance LIBs [18–20].

The electrochemical performance (especially for high rate charging/discharging) of vanadium oxides are significant based on their sophisticated electrode architectures, whose function is to expose as much surface to the electrolyte as possible, thus exhibiting extrinsic pseudocapacitive response [10–12,21–24]. The nanoarchitectures, such as nanoparticles, nanorods, nanowires (NWs) and nanosheets, have been designed to achieve high capacity of vanadium oxides, due to their large surface area and short ion diffusion pathway [25–27]. However, their rate performance is still unsatisfied. According to the $t = \lambda^2/D$ (where D is diffusivity and λ is ion diffusion length), further reducing the λ by utilizing the ultrathin geometrical properties of nanoribbons or nanosheets is an option [8]. Liquid exfoliation methods have been well developed to produce layered materials with ultrathin morphology [28,29]. However, the self-aggregation/stacking of nanomaterials

* Corresponding author at: State Key Laboratory of Advanced Technology for Materials Synthesis and Processing, International School of Materials Science and Engineering, Wuhan University of Technology, Wuhan 430070, China.
E-mail addresses: qlwei@ucla.edu (Q. Wei), mlq518@whut.edu.cn (L. Mai).
[1] These authors contributed equally to this work.

http://dx.doi.org/10.1016/j.nanoen.2017.08.011
Received 6 April 2017; Received in revised form 7 August 2017; Accepted 8 August 2017
Available online 09 August 2017
2211-2855/ © 2017 Elsevier Ltd. All rights reserved.

becomes more serious since the increased surface energy, leading to unexpected electrochemical performance [1]. The three-dimensional (3D) graphene hydrogel structure is regarded as an ideal model, which composed by cross-linked 3D graphene nanosheets frameworks [30–33]. The intertwined graphene walls offer continuous electron transport, while the interconnected porous microstructure allows easy penetration of electrolyte into the framework, leading to remarkable electrochemical performance [34]. Inspired by the 3D graphene hydrogel structure, the similar vanadium oxide hydrogel is likely to display promising properties [10,35,36], but it remains largely unexplored.

Previous works have demonstrated remarkable electrochemical performance of vanadium oxide nanomaterials, but they are usually at low mass loading level (Table S1) [12,37–41]. For the practical applications, high mass loading is necessary, but it faces the following challenges: (1) high mass loading is usually accompanied with increased thickness, leading to the difficulty of electrolyte penetration, ion diffusion and electron transport, then failing to take full utilization of active materials (especially at high rate); (2) stable cycling performance at high mass loading needs strict requirements [42]; (3) electrodes tend to delaminate from the current collectors during the coating process with high mass loading [43]. The 3D intertwined hydrogels structure shows the ability of achieving high electrochemical performance and it deserves further investigation of their properties at high mass loading level.

Herein, for the first time, we report the design of 3D vanadium oxide ($H_2V_3O_8$) hydrogels through a universal modified liquid exfoliation strategy. Compared to the electrochemical performance of normal nanowires (NWs) and pure ultrathin nanoribbons, the $H_2V_3O_8$ hydrogels display largely enhanced rate capability and cycling stability. Combining the geometrical features of hydrogels with an *in-situ* synthesis method, an intertwined hydrogels/carbon nanotubes (CNTs) flexible film is assembled, which displays remarkable high-rate performance and excellent cycling performance at high mass loading. Our work demonstrates that the novel vanadium oxide hydrogel structure is very beneficial for enhancing the electrochemical energy storage performance.

2. Experimental section

2.1. Experimental methods

2.1.1. Synthesis of vanadium oxide hydrogels

The vanadium oxide hydrogels were synthesized *via.* a facile hydrothermal method. The V_2O_5 sols (1.5 mmol), prepared by a melt quenching process as reported previously [44], were diluted with deionized water to 60 mL under magnetic stirring. The surfactant PVP K30 (17 mg) and Li_2CO_3 (0.1 mmol) were added with stirring for another 2 h and aging for one day. Then, the mixed solution was transferred into a sealed Teflon container in oven at 180 °C for 120 h and then allowed to cool to room temperature naturally. The obtained hydrogels were soaked in deionized water for 12 h with three times, and dried for further use.

2.1.2. Synthesis of vanadium oxide NWs

The nanowires (NWs) were synthesized with the only addition of PVP K30 (17 mg) and kept other same conditions for hydrogels. The obtained NWs were washed with deionized water and alcohol, and dried for further use.

2.1.3. Synthesis of vanadium oxide hydrogels/CNTs films

The mixed V_2O_5 sols, PVP K30 and Li_2CO_3 solution was prepared at first. CNTs (100 mg, multiwall, OD: 30–50 nm, L: 10–20 μm, XFNANO) was added with strongly ultrasonic treatment. After the same hydrothermal process, the hydrogels/CNTs composite was obtained. Then the composite was dispersed in 40 mL deionized water under strongly stirring. The suspension was filtrated with a nylon filter paper (pore size 1.0 μm) using vacuum filtration and washed by DI-water, leading to a flat film on the filter paper. The film with filer paper was kept in flat and dried at 40 °C. After several hours, the dried film was almost separated from filter paper, very easy to be peeled off. Finally, the film was further dried at 80 °C overnight for further use. Through controlling the filtrated volume of hydrogels/CNTs, the films with different mass loading levels were adjusted.

2.2. Materials characterization

X-ray diffraction (XRD) patterns were collected by a D8 Advance X-ray diffractometer, using Cu Kα radiation (λ = 1.5418 Å). The microstructures were observed by a Field-emission scanning electron microscopy (SEM) (JEOL-7100F), and a transmission electron microscopy (TEM) and a high-resolution TEM (HRTEM) (JEM-2100F). The atomic force microscopic (AFM) observation was achieved using a Bruker MultiMode 8 Atomic Force Microscope. X-ray photoelectron spectroscopy (XPS) measurements were obtained using a VG MultiLab 2000 instrument. Inductively Coupled Plasma (ICP) test was performed on a PerkinElmer Optima 4300DV spectrometer. CHN elemental analyzer was involved in determining the carbon contents. Brunauer-Emmet-Teller (BET) surface areas were measured by using a Tristar II 3020 instrument.

2.3. Electrochemical measurements

The electrochemical performance was characterized by assembly of coin cell (2016-type) with lithium metal as the anode in the glove-box filled with Ar atmosphere. The general cathode electrodes were composed of 70% active material, 20% acetylene black and 10% poly (tetrafluoroethylene) (PTFE) binder. The mixed clay was processed by a roll-to-roll method to get a freestanding film. Then the film was punched into circular disk (8 mm in diameter) with a mass loading of ~ 3 mg cm^{-2}. For the hydrogels/CNTs films, they were punched into the circular disk as well, with the mass loading ranging from 3.1 to 13 mg cm^{-2}. The electrolyte is consisted of 1 mol L^{-1} $LiPF_6$ in ethylene carbonate (EC)/dimethyl carbonate (DMC) (1:1 by volume). The cells were aged for 12 h before charge/discharge to ensure full absorption of the electrolyte into the electrodes. The Li||$H_2V_3O_8$/CNTs lithium-ion pouch cell was assembled in the glove box using the $H_2V_3O_8$/CNTs film cathode (~ 15 mg). The electrolyte was injected and the cell was closed using a heat sealer. Galvanostatic charge/discharge measurement was performed by a multichannel battery testing system (LAND CT2001A), the cyclic voltammometer (CV), electrochemical impedance spectroscopy (EIS) were tested with an Autolab Potentiostat Galvanostat (PGSTAT302N). All the measurements were carried out at room temperature.

3. Results and discussion

Fig. 1a schematically illustrates the synthesis process of the $H_2V_3O_8$ hydrogels and NWs. In brief, the mixed V_2O_5 sols and surfactant (PVP) are the reaction sources. After hydrothermal treatment, NWs aqueous dispersions (inset of Fig. 1b) with tens of micrometers in length are obtained (Fig. 1b and c). For the synthesis of hydrogels, the inorganic salt (Li_2CO_3) is added in the mixed reaction sources before hydrothermal reaction. The photograph (inset of Fig. 1d) shows the hydrogel shape of the obtained sample. SEM images (Fig. 1d and e) reveal that the novel hydrogels are composed of intertwined nanoribbons and self-coiled nanoscrolls. XRD patterns confirm the crystal structure of the as-synthesized samples (Fig. 2a). All the diffraction peaks are indexed to the orthorhombic $H_2V_3O_8$ (JCPDS No. 85-2401, space group: *Pnam*, a = 16.9298 Å, b = 9.3589 Å, c = 3.6443 Å, $\alpha = \beta = \gamma = 90°$), indicating a pure phase of the products [19]. A slight shift of (200) diffraction peak to lower angle and the enhanced relative intensity of

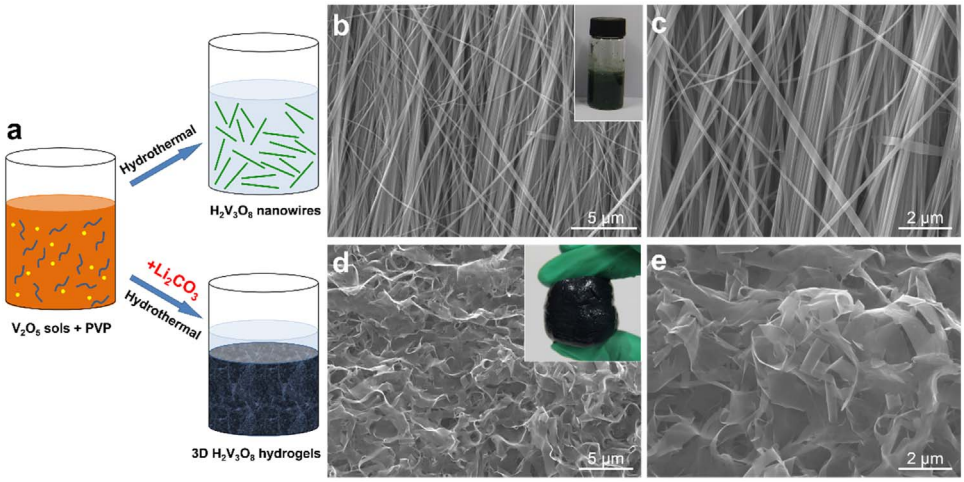

Fig. 1. (a) Schematic showing the synthesis process of the $H_2V_3O_8$ NWs and hydrogels. The $H_2V_3O_8$ NWs are obtained with surfactant (PVP), while the 3D hydrogels are formed with additional assistant of Li_2CO_3. (b, c) SEM images of the $H_2V_3O_8$ NWs, and the photograph (inset b) showing the NWs aqueous dispersions. (d, e) SEM images of the $H_2V_3O_8$ hydrogels, and the photograph (inset d) showing the hydrogel shape.

(320) and (520) peaks for hydrogels are observed, which are probably due to the pre-intercalated Li^+ ions into the $H_2V_3O_8$ layered during the hydrothermal process [16]. Additionally, the ICP analysis identifies the existence of Li element in the hydrogel sample, while the Li/V ratio is 0.067:1. The valence states of vanadium for two samples were further characterized by XPS. The Li 1s peak is weak (Fig. S1) since its amount is extremely small. Fig. 2b displays the XPS V 2p spectra, which can be divided into two peaks. The peaks centered at 517.45 and 524.75 eV correspond to the V $2p_{3/2}$ and V $2p_{1/2}$ of V^{5+}, respectively [45]. The peaks at 516.05 and 523.35 eV correspond to the V $2p_{3/2}$ and V $2p_{1/2}$ of V^{4+}, respectively [20,45]. The XPS data confirm the mixed valence states of vanadium. Calculated from the integration of the V 2p peaks, the valence ratio of V^{5+}: V^{4+} for NWs is 1.99: 1, which is close to the theoretical ratio of $H_2V_3O_8$ (V^{5+}: V^{4+} = 2:1, the average vanadium valence is 4.667). The ratio for hydrogels decreases to 1.83: 1.17, indicating the reduced valence of vanadium state (average vanadium valence is ~ 4.61). As identified by the ICP analysis, the chemical formula of hydrogels can be noted as $Li_{0.2}H_2V_3O_8$ (suggesting that the average valence of vanadium is 4.60), which is consistent with the XPS results. These data indicate that the reduced vanadium valence is attributed to the influence of Li^+ ions, while the phase of layered $H_2V_3O_8$ is still remained.

Nitrogen adsorption/desorption isotherms were generated to investigate the Brunauer-Emmet-Teller (BET) surface area and the porous structure of the samples, as shown in Fig. 2c. The adsorption-desorption curve of hydrogels displays obvious hysteresis loop (type-IV) compared to that of NWs, confirming the porous structure of 3D hydrogels [46]. The BET surface area of hydrogels and NWs is 23.1 and 19.8 $cm^2 g^{-1}$, respectively.

TEM images were further collected to investigate the microscopic structure information in detail. TEM images of hydrogels (Fig. 3a–d) show the ultrathin geometrical feature of nanoribbons and nanoscrolls. HRTEM image of a nanoribbon (Fig. 3b) displays the lattice spacings of 0.63 and 0.34 nm, corresponding to the (210) and (011) planes of $H_2V_3O_8$, respectively. The selected-area electron diffraction (SAED) pattern (Fig. 3c) reveals that the individual nanoribbon is single crystalline with the corresponding crystal spots of (210) and (011). The HRTEM image of a nanoscroll further provides the information about the crystal structure within the walls. Fig. 3d shows that the nanoscroll with multiwall is formed by the self-coiling of nanoribbons. A lattice of d_{200} ≈ 0.86 nm is observed, corresponding to the layer spacing of layered $H_2V_3O_8$. Combining with the TEM data, the growth direction of nanoribbons is [001] and the self-coiled nanoscrolls with the stacking along [200] [refs14,45,47]. The TEM image of NWs was also collected (Fig. S2). The lattice spacings of 0.47 and 0.34 nm correspond to the (020) and (011) planes, respectively, indicating that the growth direction of NWs is [001] [ref. 45]. AFM images (Figs. 3e and S2b) display that the thickness of a nanoribbon is only ~ 8.1 nm, while that of a NW is ~ 53.2 nm, indicating much decreased thickness for the modified liquid exfoliation method.

The formation process of the hydrogels was further investigated based on time-dependent experiments (Fig. S3). During the early state of hydrothermal process, the vanadium oxide sols transfer into large assembled sheets (Fig. S3b and c). As the reaction time increases, the nanoribbons are torn from the sheets surface, which are highly flexible and freely to be curved (Fig. S3d–f) [48]. During this process, the nanoribbons are self-coiled into nanoscrolls. Finally, the nanoribbons and nanoscrolls are intertwined with each other to form the 3D structural hydrogels (Figs. 1d and e and S3a). For the formation of $H_2V_3O_8$ NWs, the nanowire morphology is obtained from the splitting of nanosheets

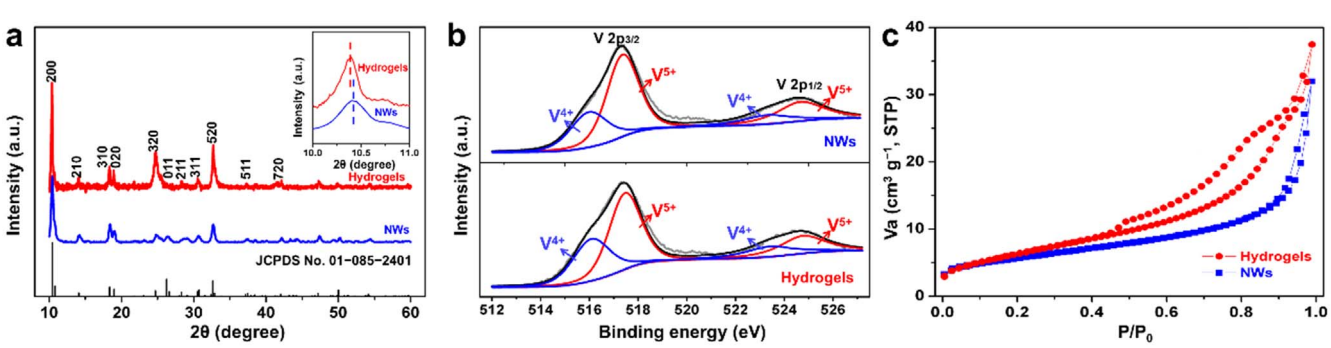

Fig. 2. (a) XRD patterns, (b) XPS V 2p spectra and (c) nitrogen adsorption-desorption isotherms of the $H_2V_3O_8$ NWs and hydrogels. The XRD patterns (inset a) showing the slight enhanced interlayer spacing of (200) and XPS spectra presenting the partly reduce of V^{5+} to V^{4+}, owing to the small amount of pre-intercalated Li^+ ions into the $H_2V_3O_8$ layers during the hydrothermal process.

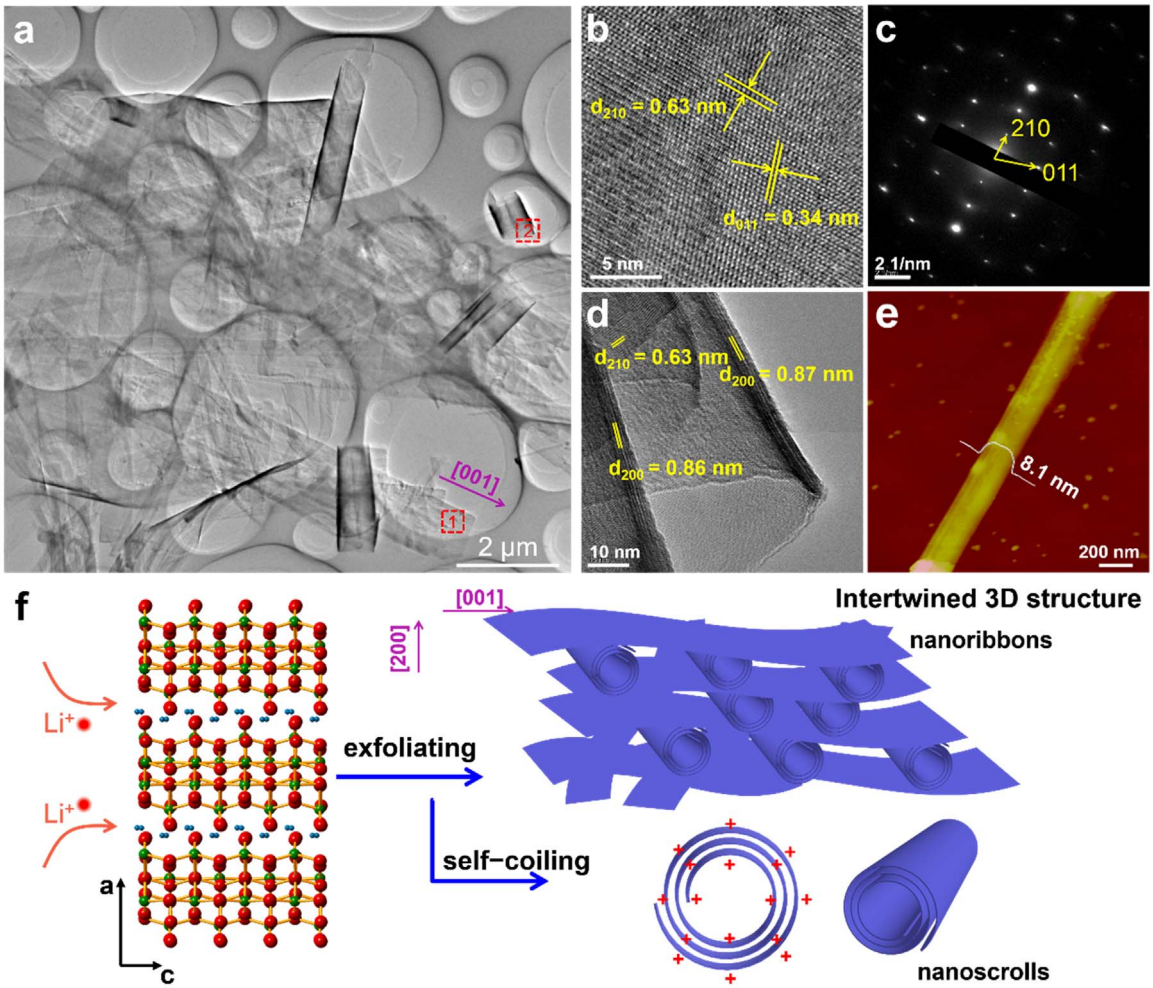

Fig. 3. (a) TEM image of $H_2V_3O_8$ hydrogels, composed of ultrathin nanoribbons and nanoscrolls. (b) HRTEM image and (c) SAED pattern of a nanoribbon (marked area 1). (d) HRTEM image of a nanoscroll (marked area 2). (e) AFM image of a nanoribbon. (f) Schematic of the forming process of nanoribbons and nanoscrolls in the $H_2V_3O_8$ 3D hydrogels. The nanoribbon/nanoscroll is growth through [001] direction with a stacking layer of [200], and the intercalated Li^+ ions promotes the forming of intertwined nanoribbons and nanoscrolls, leading to the hydrogel structure.

(Fig. S4). The NWs are formed after 48 h and still kept with longer reaction time (*e.g.* 120 h, Fig. S4d and e). As shown in Fig. 3f, the *c*-axis of $H_2V_3O_8$ is presented the shortest neighboring V–V distance, corresponding to the relatively high stacking rate along *c*-axis, resulting in the preferential growth direction of [001] for both the nanoribbons and NWs and the stacking orientation is along [200] [refs 45,48].

The Li^+ ions play an importance role in the formations of hydrogels. To further investigate this, the reaction conditions with different adding amount of Li_2CO_3 were undertaken and their XRD patterns, photographs and SEM images were collected (Fig. S5). Without the influence of Li^+ ions, NWs with pure $H_2V_3O_8$ phase are formed (Figs. 1b and S5). The $H_2V_3O_8$ hydrogel is obtained at a certain amount of Li_2CO_3. Further increasing the amount of Li_2CO_3, the morphology changes from the hydrogels then to pure nanobelts (Fig. S5c–f) while the related phase transfers from mixed $H_2V_3O_8$ and VO_2 to pure VO_2 (Fig. S5a). According to above data, the formation of hydrogel structure is based on the ion assistant liquid exfoliation mechanism [28,29]. The Li^+ ions tend to pre-intercalate into the vanadium oxide layer during the hydrothermal reaction [16]. Then, driven by the high temperature and pressure thermal force along with the assistant of pre-intercalated Li^+ ions, the repulsive force between layers is increased and the thinner nanoribbons are torn from the as-formed sheets (Fig. S3d–f) [28,29]. For the self-coiling process, the nanoribbons tend to curve or self-coil to decrease the total surface energy when their electrostatic energy is higher than the elasticity energy [14,49]. The intercalated Li^+ ions increase the electrostatic energy and then beneficial to the spontaneous polarization-induced self-coiling process [48]. Interestingly, based on the modified liquid exfoliation mechanism, other cations (such as Na^+, K^+, Mg^{2+}, Mn^{2+}, Cu^{2+} and Fe^{3+}) can also be utilized to synthesize the 3D hydrogels composed by intertwined ultrathin nanoribbons and nanoscrolls (Fig. S6). The energy-dispersive X-ray (EDX) spectra (Fig. S6) and XRD patterns (Fig. S7) display the existence of each added cations. These results indicate the universal ion assisted liquid exfoliation method for preparing vanadium oxide hydrogels.

Coin cells (2016-type) were assembled to investigate the electrochemical performance of NWs and 3D hydrogels, while metallic lithium was used as the counter electrode. The pure ultrathin nanoribbons were also synthesized as a control experiment (Fig. S8) [44]. Cyclic voltammogram (CV) curves of the $H_2V_3O_8$ hydrogels and NWs were measured at a scan rate of 0.1 mV s^{-1} in the potential window of 1.5–3.5 V, as shown in Fig. 4a. All the redox peaks represent the Li^+ ion insertion and extraction processes [13,50]. The CV curve of NWs electrode displays various redox peaks, which is the typical electrochemical behavior of $H_2V_3O_8$ [19]. Compared to the CV curve of NWs electrode, the hydrogels electrode display two major redox peaks of 2.70/2.45 and 2.21/1.85 V. The galvanostatic charge-discharge test was measured subsequently. Fig. 4b shows the different charge-discharge platforms at the specific current of 0.1 A g^{-1}, which are consistent with their CV peaks, respectively. The reversible discharge capacity of hydrogels electrode is 310 mA h g^{-1}, which is slightly higher

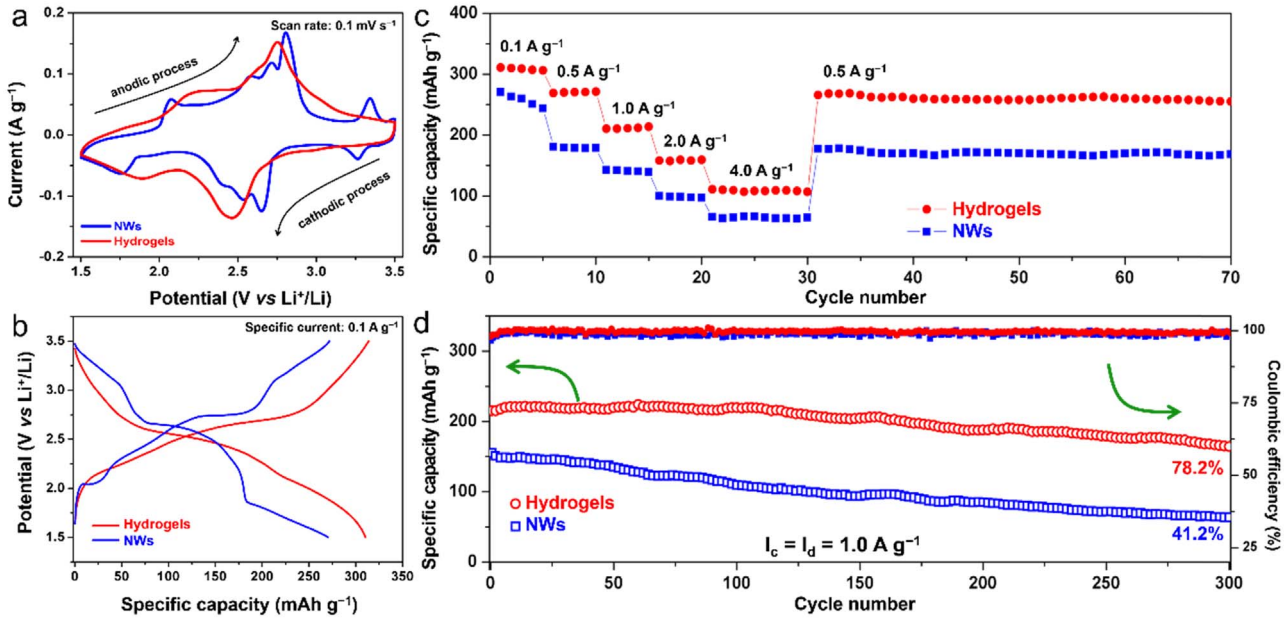

Fig. 4. (a) CV curves at a scan rate of 0.1 mV s^{-1} in a potential window of 1.5–3.5 V, (b) charge-discharge curves at a specific current of 0.1 A g^{-1}, (c) rate performance, and (d) cycling performance at 1.0 A g^{-1} of the $H_2V_3O_8$ hydrogels and NWs, respectively. The hydrogels displaying much enhanced capacity, rate capability and cycling performance than those of NWs.

than that of NWs (270 mA h g^{-1}). The change in CV and charge-discharge curves is probable due to modified morphology (ultrathin feature of nanoribbons, Fig. S8g) and structural pre-distortion caused by pre-intercalation of Li^+ ions into layered $H_2V_3O_8$. The similar phenomenon was also observed in $H_2V_3O_8$ ultrathin nanobelts, V_6O_{13} nanosheets, V_6O_{13} nanotextiles and MoO_3 nanobelts [16,44,51–53].

The rate capability is the very important performance for high-power application. Rate performance of samples at progressively increased specific current (ranging from 0.1 to 4.0 A g^{-1}) was further measured (Figs. 4c and S8h). The hydrogel electrode delivers much higher capacities than those of NWs electrode at each current, especially at high rates. The hydrogels electrode exhibits the capacities of 158 and 110 mA h g^{-1} at 2.0 and 4.0 A g^{-1}, respectively, which are ~ 1.58 and 1.70 times of the values for NWs and the much better than that of the pure nanoribbons (Fig. S8h), respectively, indicating the excellent rate capability of the 3D hydrogel structure. After the high current measurements, the hydrogels electrode recovers a capacity of 176 mA h g^{-1} at 0.5 A g^{-1} (an excellent capacity retention of 97.8%), manifesting the good rate reversibility. Long-term cycling performance at the high current of 1.0 A g^{-1} is shown in Fig. 4d. The hydrogels display a discharge capacity of 215 mA h g^{-1}, which is much higher than that of NWs (155 mA h g^{-1}). The capacity retention of hydrogels is 78.2% after 300 cycles, higher than that of NWs (41.2%) and pure ultrathin nanoribbons (Fig. S8i), indicating a better cycling performance of 3D hydrogels. Meanwhile, the coulombic efficiency remains at ~100% during the repeated charge-discharge cycles. It is found that the capacity of pure nanoribbons increases slightly in the initial tens of cycles (Fig. S8i), which is due to the gradual penetration of electrolyte into the spacing between the stacked nanoribbons. This behavior is not obvious for the hydrogels cathode (Fig. 4d) owing to the porous structure promotes the diffusion kinetics [54].

Electrochemical impedance spectra (EIS) were measured to provide further insights. As shown in Fig. S9a and b, the Nyquist plots show a depressed semicircle (representing charge transfer resistances R_{ct}) and a slanted line (representing the Warburg impedance that refers to ion diffusion ability). According to the fitting results, the R_{ct} of the hydrogels electrode is 44.2 Ω, much lower than that of NWs (87.5 Ω). The increase of R_{ct} for hydrogels after 100 and 200 cycles are much smaller than those of the NWs, indicating the stable electrode-electrolyte interface during cycling (that reflects the excellent cycling stability) [16,26]. Furthermore, the diffusion coefficient values of the Li^+ ions (D) can be calculated based on the EIS spectra by using the Eqs. (1) and (2),

$$D = 0.5(RT/n^2F^2AC\sigma)^2 \tag{1}$$

$$Z' = R_D + R_L + \sigma\omega^{-1/2} \tag{2}$$

where R is the gas constant, T is the temperature, n is the number of electron transfer per molecule during intercalation, F is Faraday's constant, A is the area of the electrode surface, C is the molar concentration of Li^+ ions, and σ is the Warburg factor. Based on the Eq. (2), the linear fitting of Z' and $\omega^{-1/2}$ is displayed in Fig. S9d [55]. From the fitting results, the σ value can be calculated for the slope. At the 10th cycles, the ratio of $\sigma_{NWs}/\sigma_{hydrogels}$ is 3.54, corresponding to $D_{hydrogels}/D_{NWs} \approx$ 12.5, which demonstrates the significantly increased Li^+ ion diffusion kinetics for the 3D hydrogels.

As pointed by Dunn and co-workers, a capacitive behavior will be enhanced with sophisticated electrode architectures whose function is to expose as much of the surface to the electrolyte as possible, noted as extrinsic pseudocapacitor [22]. According to this, a kinetics analysis based on the various increased CV scan rates (Fig. S10) was further discussed. The responded current i(V) can be separated into a diffusion contribution ($k_1\nu$) and a capacitive contribution ($k_2\nu^{1/2}$), displayed as Eq. (3).

$$i(V) = k_1\nu + k_2\nu^{1/2} \tag{3}$$

The linear plot of $i/\nu^{1/2}$ *versus* $\nu^{1/2}$ was used to determine k_1 and k_2, then the diffusion processes and those from capacitive effects can be quantified [56,57]. The data shown in Fig. S10c and d indicate that capacitive charge storage contribution in hydrogels occurs to a much greater extent compared with NWs (50% *versus* 29%) at a scan rate of 1.0 mV s^{-1}. The modified hydrogels with enhanced diffusion kinetics promote the lithium intercalation process, thus resulting in the enhanced capacitive contribution [52,58].

Beneficial from the unique geometrical features of the intertwined 3D hydrogel structure, it can be regarded as the scaffolds to *in-situ* composite other high conductive materials to modify the performance (since the electronic conductivity of vanadium oxide is not ideal).

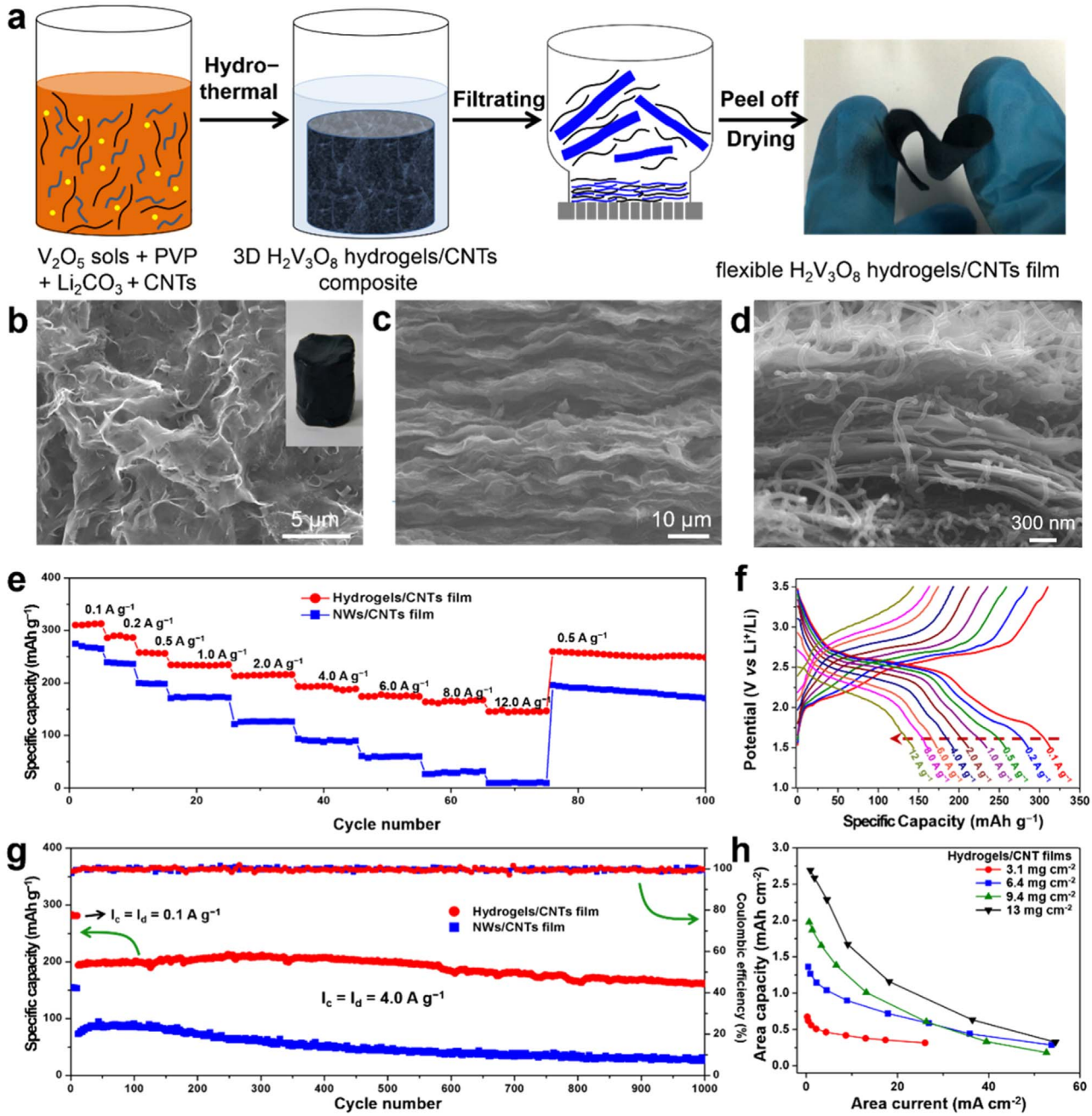

Fig. 5. (a) Schematic showing the fabrication process of the flexible $H_2V_3O_8$ hydrogels/CNTs films. The hydrogels/CNTs is prepared by an *in-situ* synthesis methods. Then through a facial vacuum-assisted filtrating process, the flexible hydrogels/CNTs film is obtained. (b) SEM image of the $H_2V_3O_8$ hydrogels/CNTs composite. (c, d) Cross-sectional SEM images of the hydrogels/CNTs film, showing the uniform layer-by-layer structure. (e) Rate performance of the hydrogels/CNTs and NWs/CNTs films. (f) Charge-discharge curves of the hydrogels/CNTs film at various specific currents. (g) Cycling performance at 4.0 A g^{-1}. (h) Area capacity *vs.* area current plots. The excellent performance at high mass loading indicating the effective design of the hydrogels/CNTs flexible films.

Moreover, the addition of non-conductive binders and dispersive conductive carbon nanoparticles will increase the charge transfer resistance and hinder the full utilization of their high surface, failing to achieve preconceived high rate performance [20,45]. In this case, a binder-free flexible film is further fabricated to achieve better rate performance, while the long CNTs are selected as the conductive additive owing to the long-range conductivity and high mechanical robustness [47,59]. As illustrated in Fig. 5a, an *in-situ* synthesis approach is processed to combine the geometrical features of hydrogels and CNTs, and then an intertwined vanadium oxide hydrogels/CNTs flexible film (binder-free) is obtained. Simply, the CNTs are directly dispersed in the reaction resources with strong ultrasonic treatment, while the PVP surfactant and negative charge of V_2O_5 sols improve the dispersion of CNTs. After hydrothermal, the hybrid vanadium oxide hydrogels/CNTs composite (inset of Fig. 5b) is obtained. The SEM images (Figs. 5b and S11) show that the hybrid hydrogels are composed by the nanoribbons, nanoscrolls and the uniform distribution of CNTs. Further through the vacuum-assisted filtrating of the vanadium oxide hydrogels/CNTs composite, the flexible vanadium oxide hydrogels/CNTs film is obtained. An obvious layer-by-layer structure is confirmed by the SEM image (Fig. 5c), while the CNTs are uniformly distributed in between the vanadium oxide layers (Fig. 5d). The mass loading of the hydrogels/CNTs film is ~ 3.1 mg cm^{-2} with a thickness of ~ 40 μm (Fig. S12). The *in-situ* synthesis of $H_2V_3O_8$ NWs/CNTs composite was

also prepared, while non-hydrogel structure is obtained as well and the distribution of CNTs is ununiformed (Fig. S13). The XRD patterns (Fig. S14a) of the hydrogels/CNTs and NWs/CNTs films confirm the $H_2V_3O_8$ phase, while an additional strong diffraction peak at ~ 26° is from the CNTs. Raman spectrum of the film (Fig. S14b) displays very strong G band (graphitic carbon) peak, which indicates the highly conductivity of CNTs. The content of CNTs for the composites is 30% determined by the CHN element analysis.

The flexible films were directly cut into small rounds for the electrochemical performance testing. The capacity is calculated based on the weight of active material, while the CNTs deliver negligible capacity in the potential range of 1.5–3.5 V (Fig. S15). As displayed in Fig. 5e and f, the hydrogels/CNTs film displays remarkable rate capability, much better than that of the NWs/CNTs film. Even at a high specific current of 12 A g^{-1}, a high capacity of 145 mA h g^{-1} is achieved, corresponding to a charge/discharge time of 43.5 s. While for the NWs/CNTs, almost no capacity is delivered at such high specific current. The related charge-discharge curve of hydrogels/CNTs film at 0.1 A g^{-1} displays a smaller overpotential (ΔV(Q/2)) than that of NWs/CNTs film (68 *vs.* 148 mV, Fig. S16). Further compared to the rate performance of hydrogels/acetylene black film (Fig. S17), the hydrogels/CNTs film delivers largely enhanced performance, because the uniform and interconnected long CNTs networks in the hydrogel provide continuous electron transport. Stable cycling of the films at high specific current (4.0 A g^{-1}) were tested (Fig. 5g). After 1000 cycles, the capacity retention of the hydrogels/CNTs film is 84.0%, much higher than that of the NWs/CNTs film (36.3%). It is noted that the hydrogels/CNTs film with a mass loading of 3.1 mg cm^{-2} still delivers very high rate capability compared to the state-of-the-art reported values [12,37–41].

Owing to the advantages of continuous electron/ion diffusion of the hydrogels/CNTs structure, it is possible to deliver high electrochemical performance with increased mass loading. Based on the facile filtrating process, the hydrogels/CNTs films with different mass loadings of 3.1, 6.4, 9.4 and 13 mg cm^{-2} were fabricated. With the increase of mass loadings, the films also deliver good rate performance (Fig. 5h). At the areal current of 0.22, 0.45, 0.66 and 0.91 mA cm^{-2}, the specific capacity of the films (mass loading from 3.1 to 13 mg cm^{-2}) is the 310, 304, 301 and 296 mA h g^{-1}, respectively, showing very small capacity loss with increased mass loading. The rate capability decreases with the mass loading, owing to the enlarged the electron/ion diffusion length [43]. The films with large mass loading show decreased areal capacity accompany with the increased areal current. However, at the same area current, thick film still exhibits larger area capacity compared to that of thinner ones, such as high areal capacities of ~ 2.70 mA h cm^{-2} at 0.91 mA cm^{-2} and ~ 1.16 mA h cm^{-2} at 18.2 mA cm^{-2} are obtained for the mass loading of 13 mg cm^{-2}. At the area currents above 20 mA cm^{-2}, the hybrid flexible films display high areal capacity, which is rarely reported for the vanadium oxide cathode. Furthermore, the flexible film with different thicknesses still display excellent cycling stability (above 84% capacity retention) over 1000 cycles (Fig. S18). The morphology of hybrid film is largely maintained after long-term cycles (Fig. S19), revealing the excellent structure stability. Furthermore, the Li||$H_2V_3O_8$/CNTs pouch cell was assembled to show the reversibility and durability of the hybrid film. As shown in Fig. S20, the pouch cell shows good reversible charge-discharge curves before and after folding and it brightens the light-emitting diode (LED) bulb chain at folded and unfolded state. These results indicate the $H_2V_3O_8$/CNTs film exhibits a good reversibility and durability [60].

On the basis of the above results, the superior high-rate capability and cycling stability of hybrid hydrogels/CNTs film are attributed to the advantages of the designed nanoarchitecture: (i) the hydrogels composed of ultrathin nanoribbons and self-coiled nanoscrolls offer largely shortened ion diffusion length; (ii) the rich pores in the hydrogels increase the electrode-electrolyte contact area and provide interconnected channels for efficient ion diffusion; (iii) the self-coiled nanoscrolls and the rich pores support the excellent mechanical robustness, leading to excellent cycling performance; (iv) the binder-free 3D intertwined hydrogels/CNTs structure endows continuous electron/ion transport [4,7].

4. Conclusion

In summary, a novel architecture of 3D vanadium oxide ($H_2V_3O_8$) hydrogel composed of intertwined nanoribbons and self-coiled nanoscrolls is successfully synthesized through a modified liquid exfoliation strategy. The developed synthesis method is universal and can be extended to prepare vanadium oxide hydrogels with various cations (including Li^+, Na^+, K^+, Mg^{2+}, Mn^{2+}, Cu^{2+} and Fe^{3+}). Comported to the electrochemical performance of NWs and nanoribbons, the $H_2V_3O_8$ hydrogels display much enhanced capacitive contribution, rate capability and cycling stability. Combining the advantages of novel 3D intertwined hydrogel architecture and conductive CNTs, the hydrogels/CNTs binder-free flexible film displays remarkable high capacity, high-rate performance and excellent cycling performance even at high mass loading level. The hybrid film with a high mass loading of 13 mg cm^{-2} delivers a high areal capacity of 2.70 mA h cm^{-2} at 0.91 mA cm^{-2} and excellent rate capacity (*e.g.* an area capacity of 1.16 mA h cm^{-2} at 18.2 mA cm^{-2}). The hybrid films also deliver excellent cycling stability over 1000 cycles. The present work demonstrates the advantages of novel transition metal oxide hydrogel structure for delivering high electrochemical performance. We believe that the novel hydrogels as the scaffolds to combine with other ion doping or functional materials can be further developed for various applications.

Acknowledgements

This work was supported by the National Key Research and Development Program of China (2016YFA0202603), the National Basic Research Program of China (2013CB934103), the National Natural Science Foundation of China (51521001, 51602239), the National Natural Science Fund for Distinguished Young Scholars (51425204), and the Fundamental Research Funds for the Central Universities (WUT: 2016III001, 2016III003, 2016IVA090), and the International Postdoctoral Exchange Fellowship Program (20160025). Prof. Liqiang Mai gratefully acknowledged financial support from China Scholarship Council (No. 201606955096).

Appendix A. Supplementary material

Supplementary data associated with this article can be found in the online version at http://dx.doi.org/10.1016/j.nanoen.2017.08.011.

References

[1] M.R. Lukatskaya, B. Dunn, Y. Gogotsi, Nat. Commun. 7 (2016) 12647.
[2] D. Larcher, J. Tarascon, Nat. Chem. 7 (2015) 19–29.
[3] M. Salanne, B. Rotenberg, K. Naoi, K. Kaneko, P.-L. Taberna, C. Grey, B. Dunn, P. Simon, Nat. Energy 1 (2016) 16070.
[4] L. Mai, X. Tian, X. Xu, L. Chang, L. Xu, Chem. Rev. 114 (2014) 11828–11862.
[5] D. Chao, C. Zhu, P. Yang, X. Xia, J. Liu, J. Wang, X. Fan, S.V. Savilov, J. Lin, H.J. Fan, Z.X. Shen, Nat. Commun. 7 (2016) 12122.
[6] B.K. Lesel, J.S. Ko, B. Dunn, S.H. Tolbert, ACS Nano 10 (2016) 7572–7581.
[7] Q. Wei, F. Xiong, S. Tan, L. Huang, E.H. Lan, B. Dunn, L. Mai, Adv. Mater. (2017), http://dx.doi.org/10.1002/adma.201602300.
[8] Y. Tang, Y. Zhang, W. Li, B. Ma, X. Chen, Chem. Soc. Rev. 44 (2015) 5926–5940.
[9] L.L. Zhang, Z. Li, X.-L. Yang, X.-K. Ding, Y.-X. Zhou, H.-B. Sun, H.-C. Tao, L.-Y. Xiong, Y.-H. Huang, Nano Energy 34 (2017) 111–119.
[10] J. Zhu, L. Cao, Y. Wu, Y. Gong, Z. Liu, H.E. Hoster, Y. Zhang, S. Zhang, S. Yang, Q. Yan, P.M. Ajayan, R. Vajtai, Nano Lett. 13 (2013) 5408–5413.
[11] C. Wu, F. Feng, Y. Xie, Chem. Soc. Rev. 42 (2013) 5157–5183.
[12] D. Chao, C. Zhu, X. Xia, J. Liu, X. Zhang, J. Wang, P. Liang, J. Lin, H. Zhang, Z.X. Shen, H.J. Fan, Nano Lett. 15 (2015) 565–573.
[13] J. Prado-Gonjal, B. Molero-Sánchez, D. Ávila-Brande, E. Morán, J.C. Pérez-Flores, A. Kuhn, F. García-Alvarado, J. Power Sources 232 (2013) 173–180.
[14] A. Pan, H.B. Wu, L. Yu, X.W.D. Lou, Angew. Chem. Int. Ed. 125 (2013) 2282–2286.
[15] H.B. Wu, A. Pan, H.H. Hng, X.W.D. Lou, Adv. Funct. Mater. 23 (2013) 5669–5674.
[16] X. Tian, X. Xu, L. He, Q. Wei, M. Yan, L. Xu, Y. Zhao, C. Yang, L. Mai, J. Power

Sources 255 (2014) 235–241.
[17] B. Yan, X. Li, Z. Bai, Y. Zhao, L. Dong, X. Song, D. Li, C. Langford, X. Sun, Nano Energy 24 (2016) 32–44.
[18] C. Zhang, H. Song, C. Zhang, C. Liu, Y. Liu, G. Cao, J. Phys. Chem. C 119 (2015) 11391–11399.
[19] Q. An, J. Sheng, X. Xu, Q. Wei, Y. Zhu, C. Han, C. Niu, L. Mai, New J. Chem. 38 (2014) 2075–2080.
[20] D. Wang, Q. Wei, J. Sheng, P. Hu, M. Yan, R. Sun, X. Xu, Q. An, L. Mai, Phys. Chem. Chem. Phys. 18 (2016) 12074–12079.
[21] Y. Yan, B. Li, W. Guo, H. Pang, H. Xue, J. Power Sources 329 (2016) 148–169.
[22] V. Augustyn, P. Simon, B. Dunn, Energy Environ. Sci. 7 (2014) 1597–1614.
[23] Y.L. Cheah, R. von Hagen, V. Aravindan, R. Fiz, S. Mathur, S. Madhavi, Nano Energy 2 (2013) 57–64.
[24] S. Liang, Y. Hu, Z. Nie, H. Huang, T. Chen, A. Pan, G. Cao, Nano Energy 13 (2015) 58–66.
[25] L. Mai, Q. An, Q. Wei, J. Fei, P. Zhang, X. Xu, Y. Zhao, M. Yan, W. Wen, L. Xu, Small 10 (2014) 3032–3037.
[26] Q. An, Q. Wei, P. Zhang, J. Sheng, K.M. Hercule, F. Lv, Q. Wang, X. Wei, L. Mai, Small 11 (2015) 2654–2660.
[27] Q. An, Q. Wei, L. Mai, J. Fei, X. Xu, Y. Zhao, M. Yan, P. Zhang, S. Huang, Phys. Chem. Chem. Phys. 15 (2013) 16828–16833.
[28] X. Zhang, Y. Xie, Chem. Soc. Rev. 42 (2013) 8187–8199.
[29] V. Nicolosi, M. Chhowalla, M.G. Kanatzidis, M.S. Strano, J.N. Coleman, Science 340 (2013) 1226419.
[30] Y. Xu, Z. Lin, X. Huang, Y. Wang, Y. Huang, X. Duan, Adv. Mater. 25 (2013) 5779–5784.
[31] C.Y. Foo, A. Sumboja, D.J.H. Tan, J. Wang, P.S. Lee, Adv. Energy Mater. 4 (2014) 1400236.
[32] Y. Wang, X. Yang, L. Qiu, D. Li, Energy Environ. Sci. 6 (2013) 477–481.
[33] Y. Xu, Z. Lin, X. Zhong, X. Huang, N.O. Weiss, Y. Huang, X. Duan, Nat. Commun. 5 (2014) 4554.
[34] Y. Xu, Z. Lin, X. Huang, Y. Liu, Y. Huang, X. Duan, ACS Nano 7 (2013) 4042–4049.
[35] G. Fang, J. Zhou, C. Liang, Y. Cai, A. Pan, X. Tan, Y. Tang, S. Liang, J. Mater. Chem. A 4 (2016) 14408–14415.
[36] J. Zhou, Q. Liang, A. Pan, X. Zhang, Q. Zhu, S. Liang, G. Cao, J. Mater. Chem. A 2 (2014) 11029–11034.
[37] J.W. Lee, S.Y. Lim, H.M. Jeong, T.H. Hwang, J.K. Kang, J.W. Choi, Energy Environ. Sci. 5 (2012) 9889–9894.
[38] B. Yan, X. Li, Z. Bai, M. Li, L. Dong, D. Xiong, D. Li, J. Alloy. Compd. 634 (2015) 50–57.
[39] Y. Sun, S.-B. Yang, L.-P. Lv, I. Lieberwirth, L.-C. Zhang, C.-X. Ding, C.-H. Chen, J. Power Sources 241 (2013) 168–172.
[40] Y. Su, A. Pan, Y. Wang, J. Huang, Z. Nie, X. An, S. Liang, J. Power Sources 295 (2015) 254–2258.
[41] M. Qin, Q. Liang, A. Pan, S. Liang, Q. Zhang, Y. Tang, X. Tan, J. Power Sources 268 (2014) 700–705.
[42] N. Liu, Z. Lu, J. Zhao, M.T. McDowell, H.-W. Lee, W. Zhao, Y. Cui, Nat. Nanotechnol. 9 (2014) 187–192.
[43] L. Hu, F. La Mantia, H. Wu, X. Xie, J. McDonough, M. Pasta, Y. Cui, Adv. Energy Mater. 1 (2011) 1012–1017.
[44] Q. Wei, S. Tan, X. Liu, M. Yan, F. Wang, Q. Li, Q. An, R. Sun, K. Zhao, H. Wu, L. Mai, Adv. Funct. Mater. 25 (2015) 1773–1779.
[45] H. Li, T. Zhai, P. He, Y. Wang, E. Hosono, H. Zhou, J. Mater. Chem. 21 (2011) 1780–1787.
[46] S. Wu, W. Chen, L. Yan, J. Mater. Chem. A 2 (2014) 2765–2772.
[47] Y. Xue, X. Zhang, J. Zhang, J. Wu, Y. Sun, Y. Tian, Y. Xie, J. Mater. Chem. 22 (2012) 2560–2565.
[48] K. Xu, S. Hu, C. Wu, C. Lin, X. Lu, L. Peng, J. Yang, Y. Xie, J. Mater. Chem. 22 (2012) 18214–18220.
[49] P.P. Wang, Y. Yang, J. Zhuang, X. Wang, J. Am. Chem. Soc. 135 (2013) 6834–6837.
[50] J.B. Cook, H.-S. Kim, Y. Yan, J.S. Ko, S. Robbennolt, B. Dunn, S.H. Tolbert, Adv. Energy Mater. 6 (2016) 1501937.
[51] L.Q. Mai, B. Hu, W. Chen, Y. Qi, C. Lao, R. Yang, Y. Dai, Z.L. Wang, Adv. Mater. 19 (2007) 3712–3716.
[52] H.-S. Kim, J.B. Cook, H. Lin, J.S. Ko, S.H. Tolbert, V. Ozolins, B. Dunn, Nat. Mater. 16 (2017) 454–460.
[53] Y.L. Ding, Y. Wen, C. Wu, P.A. van Aken, J. Maier, Y. Yu, Nano Lett. 15 (2015) 1388–1394.
[54] X. Chen, H. Zhu, Y.C. Chen, Y. Shang, A. Cao, L. Hu, G.W. Rubloff, ACS Nano 6 (2012) 7948–7955.
[55] J. Hu, Y. Jiang, S. Cui, Y. Duan, T. Liu, H. Guo, L. Lin, Y. Lin, J. Zheng, K. Amine, F. Pan, Adv. Energy Mater. 6 (2016) 1600856.
[56] J.B. Cook, H.-S. Kim, T.C. Lin, C.-H. Lai, B. Dunn, S.H. Tolbert, Adv. Energy Mater. (2016) 1601283.
[57] Z. Le, F. Liu, P. Nie, X. Li, X. Liu, Z. Bian, G. Chen, H.B. Wu, Y. Lu, ACS Nano 11 (2017) 2952–2960.
[58] Y. Zhao, J. Feng, X. Liu, F. Wang, L. Wang, C. Shi, L. Huang, X. Feng, X. Chen, L. Xu, M. Yan, Q. Zhang, X. Bai, H. Wu, L. Mai, Nat. Commun. 5 (2014) 4565.
[59] L. Mai, Q. Wei, Q. An, X. Tian, Y. Zhao, X. Xu, L. Xu, L. Chang, Q. Zhang, Adv. Mater. 25 (2013) 2969–2973.
[60] Y. Hu, X. Sun, J. Mater. Chem. A 2 (2014) 10712–10738.

Yuhang Dai is an undergraduate student and in Department of Materials Science of Engineering from Wuhan University of Technology since 2014. His current research focuses on the energy storage materials and devices.

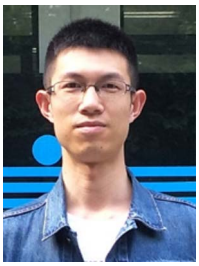

Qidong Li received his M.S. degree in Materials Engineering from Wuhan University of Technology in 2015. He is currently working toward the Ph.D. degree and his current research focuses on the energy storage materials and devices.

Shuangshuang Tan received his B.S. degree in Material Science and Engineering from Wuhan University of Technology in 2016. He is currently working toward the Ph.D. degree and his current research focuses on the energy storage materials and devices.

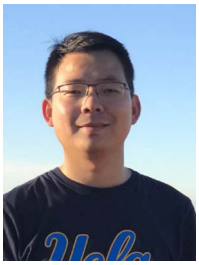

Qiulong Wei received his Ph.D. from the State Key Laboratory of Advanced Technology for Materials Synthesis and Processing, Wuhan University of Technology in 2016, under the supervision of Prof. Qingjie Zhang and Prof. Liqiang Mai. Currently, he is a postdoctoral fellow in Prof. Bruce Dunn Group at the Materials Science and Engineering department, UCLA. His current research involves the design and synthesis of nanomaterials for achieving both high energy density and power density, electrochemical energy storage devices.

Yexin Pan is an undergraduate student and in Department of Materials Science of Engineering from Wuhan University of Technology since 2014. His current research focuses on the energy storage materials and devices.

Xiaocong Tian received his first B.S. degree in material physics from Wuhan University of Technology, China in 2011 and second B.S. degree in English from Huazhong University of Science & Technology, China, in the same year. In 2016, he was awarded his Ph.D. degree in materials science and engineering from Wuhan University of Technology, where he worked under the supervision of Prof. Liqiang Mai. He is currently a postdoctoral research fellow working with Prof. Kun Zhou at the Singapore Centre for 3D Printing, Nanyang Technological University, Singapore. His research interests include 3D printing, novel nanomaterials, and energy-related devices

Kangning Zhao received his B.S. degree in Department of Materials Science of Engineering from Wuhan University of Technology in 2012. He has joined WUT-Harvard Joint Nano Key Laboratory for two years. He is currently working toward the Ph.D. degree. His current research involves the nanomaterials achieving high energy density and power density for lithium ion battery and sodium ion battery.

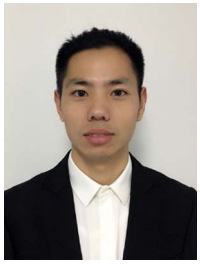

Xu Xu is Assistant research fellow of Materials Science and Engineering at Wuhan University of Technology (WUT). He received his Ph.D. degree from WUT in 2016. He carried out his postdoctoral research in Professor Xiangfeng Duan's group at University of California, Los Angeles in 2014–2016. Currently, his research interest includes energy storage materials and devices.

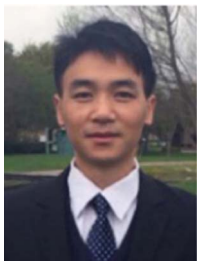

Qinyou An is Associate Professor of Materials Science and Engineering at Wuhan University of Technology (WUT). He received his Ph.D. degree from WUT in 2014. He carried out his postdoctoral research in the laboratory of Prof. Yan Yao at the University of Houston in 2014–2015. Currently, his research interest includes energy storage materials and devices.

Liqiang Mai is Chair Professor of Materials Science and Engineering at Wuhan University of Technology (WUT). He is Cheung Kong Scholar Chair Professor and the winner of the National Natural Science Fund for Distinguished Young Scholars. His current research interests focus on new nanomaterials for electrochemical energy storage and micro/nano energy devices. He received his Ph.D. degree from WUT in 2004. He carried out his postdoctoral research in the laboratory of Prof. Zhonglin Wang at Georgia Institute of Technology in 2006–2007 and worked as advanced research scholar in the laboratory of Prof. Charles M. Lieber at Harvard University in 2008–2011. He worked as advanced research scholar in the laboratory of Prof. Peidong Yang at University of California, Berkeley in 2017.

Qingjie Zhang received his Ph.D. from Huazhong University of Science and Technology in 1990. His research focuses on thermoelectric materials and related applications. At present, he is the Director of State Key Laboratory of Advanced Technology for Materials Synthesis and Processing at the Wuhan University of Technology (2005 – present) as well as the Chief Scientist of National 973 Program (2007 – 2017) in the field of thermoelectric materials.